# **Simplify** your imaging workflows

## Make research imaging workflows accessible, traceable, and secure with Athena Software for Core Imaging Facilities.

Thermo Scientific™ Athena Software is a premium imaging data management platform designed for core imaging facilities that support materials science research.

Athena Software ensures traceability of images, metadata, and experimental workflows through an intuitive and collaborative web interface.

Find out more at **thermofisher.com/athena**

ThermoFisher SCIENTIFIC

ADVANCED OPTICAL MATERIALS
www.advopticalmat.de

# Structural Coloration by Internal Reflection and Interference in Hydrogel Microbubbles and Their Precursors

*Hong Chen, Hong Zhu, Yunqi Wang, Jinrun Liu, Yang Wang, Xinhua Hu,* Alexander A. Solovev, Gaoshan Huang,* and Yongfeng Mei*

**Compound microbubbles with engineered shells, fabricated by microfluidic techniques, have drawn considerable interest for interdisciplinary research, including ultrasound imaging agents, chemical micromotors, and optical microcavities. Meanwhile, though vastly investigated, dynamic shell thickness variations of microbubbles can be hardly calculated via conventional techniques. Here the fabrication of colorful microbubbles encapsulated in hydrogel precursor using glass-capillary microfluidic methods is demonstrated. The proposed optical geometrical model elucidating the structural coloration is used for thickness assessment. Thin-film interference occurring upon illumination of the microbubble shell is found to be responsible for the coloration. The interfered lights travel along with the shell interfaces through total internal reflection in microbubbles with buoyancy-induced asymmetric shell. A concise thickness evaluation methodology provided by the established model predicts the thickness evolution of microbubbles. These results demonstrate tunable optical properties of shin-shell compound microbubbles for potential applications in displays, sensing, and anti-counterfeiting materials.**

## 1. Introduction

Gas encapsulated in a layer of thin shell constitutes an ubiquitous configuration as soap bubbles. Macroscopic soap bubbles exhibit iridescent colors while illuminated by broadband light sources because of the angle-dependent thin-film interference at the refractive-index mismatched interfaces.[1] As the dimensions of similar structures decrease to microns, the microbubbles can be utilized as optical resonators,[2–4] microlenses,[5] and optical actuators,[6,7] thanks to the refractive-index differences and the structural confinement. Microspheres and microdroplets, consisting of fine structures and anisotropic refractive indexes, can exhibit vivid colors macroscopically and microscopically.[8–12] The colorations originate from interference and diffraction in photonic crystals,[8,9] selective Bragg reflection in cholesteric liquid crystals,[10,11] and interference enabled by total internal reflection (TIR) along with the micro-concave interfaces.[12] Because of the involved TIR processes, colorful annular patterns can be observed within single microdroplets,[10–12] which are also found in shelled microbubbles instead of macroscopic soap bubbles.

Besides these, the gas-in-liquid/solid encapsulation has various applications in drug delivery,[13,14] ultrasound contrast agent,[13,15,16] and functional hierarchical structure fabrication.[17,18] To get more insight into the evolution and stability of the structure, dynamic behaviors of bubble evolution as a result of film drainage and rupture, with scales from meters to nanometers, have been extensively studied.[19–23] To evaluate bubbles' evolution, radius and shell thickness are the commonly used structural parameters, while bubbles' shell thickness can hardly be accurately measured by normal optical microscope.[23,24] At present, different techniques have been proposed and implemented to monitor the film thickness's alteration.[24,25] For instance, interferometry is engaged to analyze the fringes formed by the interference of reflected light from the thin film's two interfaces. Though the technique can measure the film thickness over a large area in a real-time manner, it can hardly provide more geometrical information about an evolving microbubble as a whole.[24]

Here we report the fabrication of precursor-microbubbles and the coloration patterns within individual microbubbles in reflection mode. The shelled microbubbles were produced by glass-capillary microfluidic chips and can be UV-cured for conservation. A geometrical model was proposed to account for the generation of colors and verified based on the coloration's dynamic variation. It is proved that thin-film interference and total internal reflection are combined within the microstructure to enable the colored retroreflection of lights. The model can be employed for thickness evaluation of microbubbles floating in a liquid environment. We consider that our research can be engaged in fabricating structural-color microbubbles and therefore, should have a great potential in hierarchical functional shell-like structures with structural coloration.

H. Chen, H. Zhu, Y. Q. Wang, J. R. Liu, Y. Wang, Prof. X. H. Hu, Prof. A. A. Solovev, Prof. G. S. Huang, Prof. Y. F. Mei
Department of Materials Science
Fudan University
220 Handan Road, Shanghai 200433, P. R. China
E-mail: huxh@fudan.edu.cn; gshuang@fudan.edu.cn

The ORCID identification number(s) for the author(s) of this article can be found under https://doi.org/10.1002/adom.202100259.

DOI: 10.1002/adom.202100259

 

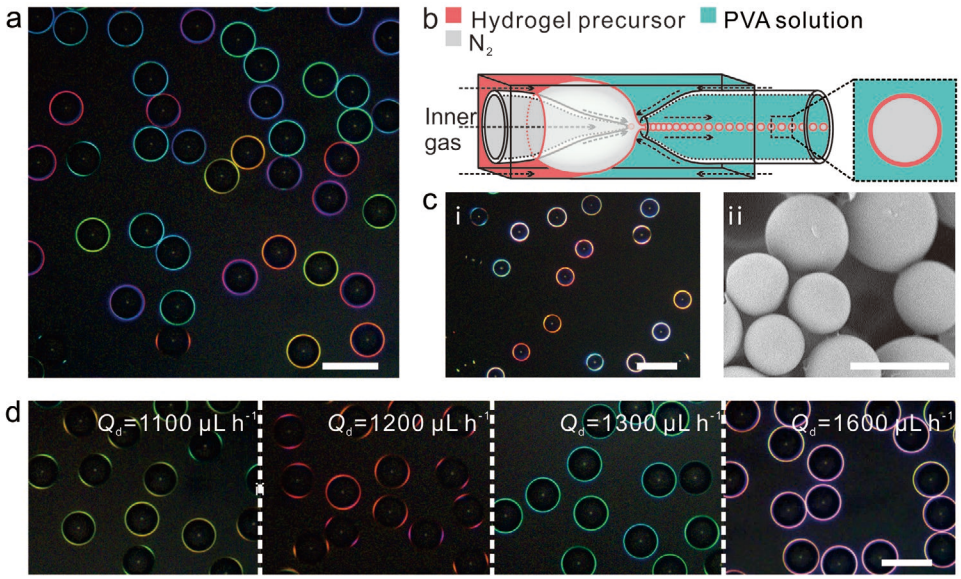


**Figure 1.** a) Reflection microscope image of colorful precursor-microbubbles under 10× objective. The scale bar is 100 μm. b) Schematic diagram of glass capillary microfluidic chip configuration. c) Microscope image of cured microbubbles with colorful annular patterns (i) and SEM image of intact cured microbubbles (ii). The scale bars in (i) and (ii) are 100 and 30 μm, respectively. d) Colorful precursor-microbubble regulation through adjusting the flow rate of the dispersed phase ($Q_d$). The flow rate of the continuous outer phase ($Q_c$) was set at 40 000 μL $h^{-1}$ with inner gas pressure ($P_i$) fixed at 15 psi. The scale bar is 50 μm.

## 2. Results and Discussion

### 2.1. Controlled Fabrication of Microbubbles Exhibiting Colorful Annular Patterns

Structural coloration was observed in microbubbles shelled by photocurable hydrogel precursor, as shown in **Figure 1**a. In our work, shelled microbubbles were generated through the glass capillary microfluidic chip,[26] and the schematic diagram of the process is depicted in Figure 1b. With two tapered capillaries coaxially aligned in an encapsulating square tube, the chip could receive inflows of three phases, nitrogen (refractive index $n_g = 1.0$), 4 wt% polyvinyl alcohol (PVA) aqueous solution (refractive index $n_c \approx 1.34$) and hydrogel precursor (refractive index $n_d \approx 1.46$) consisting of methacrylic anhydride (MAAn), ethylene glycol dimethacrylate (EGDMA), and 2-hydroxy-2 methyl propiophenone (photo-initiator). While influx, shear forces provided by the continuous outer stream directly broke inner gas flow together with the surrounding dispersed phase into precursor-microbubbles at the outlet tube's orifice.[27] Generated precursor-microbubbles were then collected in a dish of PVA aqueous solution. As indicated in the Laplace equation, gas cores of shelled bubbles tend to be expelled to dissolve in the surrounding medium due to high inner gas pressure.[28] The addition of PVA improves the stability of the shelled structures by lowering the water–oil interfacial tension.[13] Typically, bubbles tend to gather at crescent liquid surfaces because of buoyancy and finally get ruptured.[29,30] Then, a piece of cover glass was placed atop the water surface, which flattened the interface and avoided fast bubble rupture.[30,31] Generated precursor-microbubbles capped by the cover glass were cured by UV light, and the cured microbubbles (i.e., hydrogel microbubbles) are shown in panel (i) and (ii) of Figure 1c. Obviously, the cured microbubbles also demonstrate bright coloration, indicating the possibility of the controlled fabrication of colorful microbubbles. Scanning electron microscope (SEM) image of the sample suggests that the microbubbles varied in size due to inner pressure differences and gas convection between adjacent bubbles (see panel (ii) of Figure 1c).[13]

The multiple-phase fluid configuration at the channel junction can be regulated due to the parameter-adjustable influx devices as syringe pumps. The flow rate of continuous phase $Q_c$ was first kept at 40 000 μL $h^{-1}$. Colorful annular patterns exhibited by precursor-microbubbles can be varied through adjusting the dispersed phase flow rates $Q_d$, as shown in Figure 1d and Figure S1, Supporting Information. With the fixed $Q_c$ and the increase of $Q_d$, the shell thickness of precursor-microbubbles increased[32] and the color of precursor-microbubbles varied accordingly. It is worth noting that the precursor-microbubble size had no significant changes, suggesting the structural coloration should be correlated to the shell thickness of precursor-microbubbles.

### 2.2. Theoretical Model and the Coloration Mechanism

The fabricated precursor-microbubbles were observed using an optical microscope with a 50× objective. Here, the illuminating area, shown as the white dotted line in **Figure 2**a, can be controlled by the microscope's field diaphragm. Interestingly, as the precursor-microbubble is located inside the illumination region shown in Figure 2a (i), a vivid, colorful annular pattern can be seen, indicating light emanating from the edge of the microbubble. However, when the microbubble is partially illuminated (Figure 2a (ii)), light emits only from the microbubble's

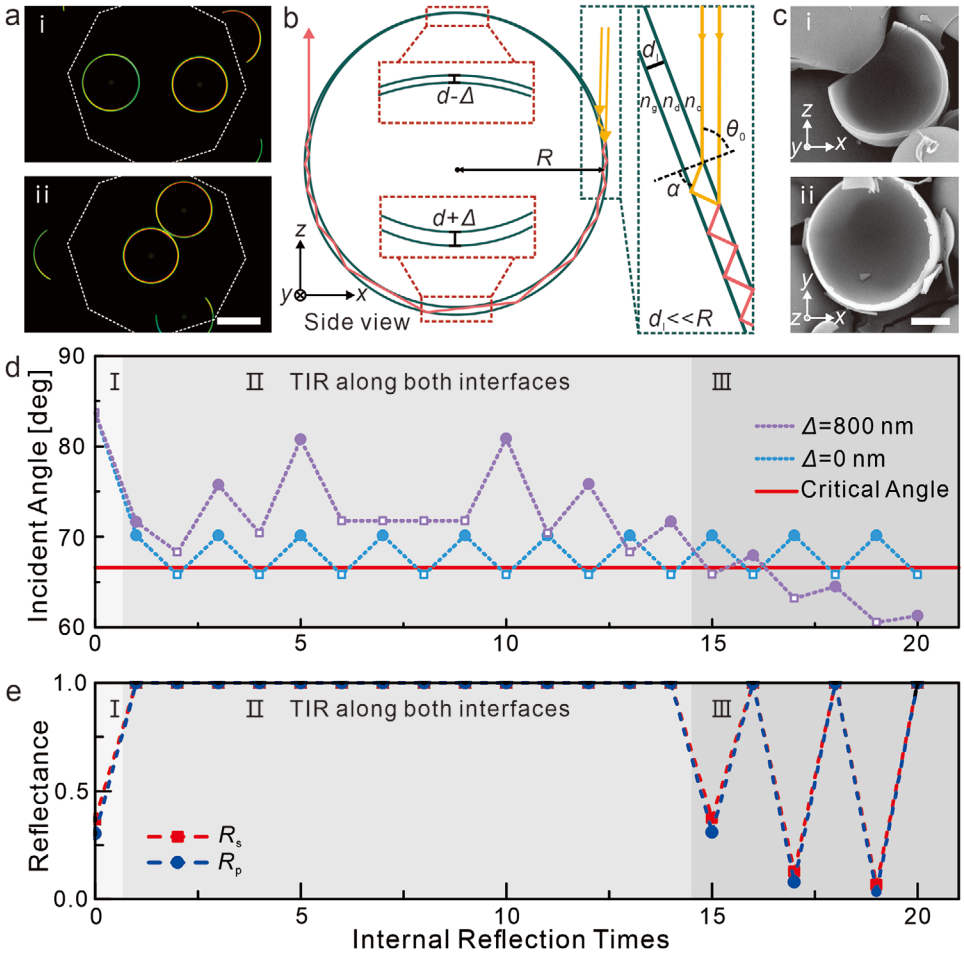


**Figure 2.** a) Optical microscope images (50×) with the observing precursor-microbubble inside the illuminating area (i) and partially moved outside the region (ii) defined by the field diaphragm (white dash line). The scale bar is 50 µm. b) Schematic illustration of a precursor-microbubble's side profile with the supposed light trace within the structure. c) SEM images of side (i) and top (ii) views of cured microbubbles. The scale bar is 10 µm. d) Variation of incident angles according to internal reflection times within shells of precursor-microbubbles with different deflections assumed ($\Delta = 0$ nm, 800 nm). Circles (•) and squares (▫) indicate reflections at the oil–gas interface and the water–oil interface, respectively. The critical angle at the water–oil interface is indicated by the red line, while the critical angle at the oil-gas interface is 43.23°. e) The reflectance of two polarization states ($R_s$, $R_p$) as light traveling inside the precursor-microbubble ($\Delta = 800$ nm). Zero-point (I) stands for the transmission point of the incoming light at the outer shell. Region II indicates that TIR is satisfied at both interfaces. In region III, the incident angles of the outer shell's reflections are smaller than the critical angle.

part outside the illumination region. Such effects suggest that structural coloration and retroreflection simultaneously occur in the microbubbles, which cannot be observed in macroscopic soap bubbles.

We introduce a geometrical optical model to account for the observed phenomena, as shown in Figure 2b. Since the Bond number of microbubbles is far less than 1,[33,34] the outer and inner surfaces of a precursor-microbubble's shell are considered as two spheres with radii $R$ and $R - d$, respectively, where $d$ is the average shell thickness. As the shell material is in liquid state, the density mismatch between the shell material and the encapsulated gas core, and the corresponding buoyancy difference can induce a vertical deflection $\Delta$ between the spherical centers.[35] Therefore, the shell thickness is $d - \Delta$ at the top and $d + \Delta$ at the bottom. Such an asymmetric shell with non-uniform thickness can be verified by SEM images (Figure 2c; Figure S2, Supporting Information).

We then consider a ray emitting from the top left of the microbubble along the $z$-axis. According to the optical path's reversibility, we can trace back the incident ray and its optical path in the shell of the microbubble (Figure 2b). It is found that multiple nearly parallel incident rays can enter the shell and finally merge into a single outgoing ray (details in Figure S3, Supporting Information). When the incident rays are monochromatic and coherent, the intensity of the outgoing light can be written as[36]

$$I = I_0 T_1 \left| \sum_{j=1}^{N} q^{j-1} \right|^2 \quad (1)$$

where $I_0$ is the intensity of incident light, $T_1$ is the total transmittance for the ray with the shortest path in the spherical shell, $q = r_{23} r_{21} \exp(i2n_d k d_i \cos\alpha)$ is the ratio of the complex

amplitudes of two adjacent incident rays, $k = 2\pi/\lambda$ is the vacuum wave vector, $n_d \approx 1.46$ is the refractive index of shell, and $r_{23}$ and $r_{21}$ are the reflection coefficients for the initial two inner reflections. Here, $N$ is the number of incident rays considered, and a dual-beam interference model ($N = 2$) is adopted in our calculations (Figure 2b). Due to the constructive interference, the output light intensity can reach the maximum at the resonant wavelength

$$\lambda_R = 2n_d d_l \cos\alpha/m \quad (2)$$

where $d_l$ is the local shell thickness, $\alpha$ is the refraction angle, and the order number $m$ is a positive integer. Such an optical interference can explain the coloration of the microbubbles.

Here, we would like to discuss the transmittance $T_1 = |t_{in}\, t_{out} \Pi r_i|^2$, where $t_{in}$ and $t_{out}$ are the transmission coefficients for light entering and leaving from the shell. $r_i$ is the reflection coefficient of the $i$-th internal reflection, which depends on the local incident angle $\theta_i$. When the incident angle is greater than the critical angle ($\theta_i > \theta_c$), the total internal reflection can occur ($|r_i| = 1$). It can be proved that when light enters a shell with a constant thickness ($\Delta = 0$), the incident angle $\theta_i$ swings between two constant values and is always less than the critical angle ($\theta_i < \theta_c$) at the outer shell interface (Figure 2d). This should lead to large energy loss for reflections at the outer shell. On the contrary, as a ray goes into an asymmetric spherical shell ($\Delta > 0$), the incident angle $\theta_i$ can first increase and then decrease in the shell (Figure 2d; Figure S4, Supporting Information), resulting in the occurrence of total internal reflection during light propagation in the shell. The total internal reflections greatly reduce the light leakage, as can be observed in the calculated reflectance ($R_s$ and $R_p$) shown in Figure 2e. This supports the retroreflection and the vivid color patterns appearing in microbubbles, even in the case of free space coupling with relatively lower efficiency.

According to the theoretical model, the mismatched refractive indexes, the deflection of spherical centers and the shell thickness are responsible for structural coloration of retroreflected light. We should stress that the theoretical model can be extended to other similar structure. As shown in Figure S5, Supporting Information, the spectrum of double emulsion with liquid core is calculated by changing the refractive index of the core.

Moreover, it is worth noting that the coloration is based on the interference of the light and therefore, the coherence length of the light needs to be taken into consideration. Considering the coherence length of halogen lamp used is ≈1.3 µm,[37] the model should be applicable for a shell thickness less than ≈1.7 µm in a typical microbubble structure. For a thicker shell, although a spectrum can be obtained by using the model (see a typical example in Figure S6, Supporting Information, where the optical path difference is larger than the coherence length), remarkable deviation should exist in the experiment.

### 2.3. Determination of the Factors Affecting the Colors Based on the Theoretical Model

The above theory shows that the color of precursor-microbubbles is related to the local shell thickness $d_l$ at the microbubble's lateral edge (where light enters the shell), which is close to the average thickness $d$ of the shell. When the average shell thickness $d$ changes, the color of the microbubbles will change, which has been demonstrated by the experiments with flow rate modulation (Figure 1d). Besides, the lateral edge shell thickness $d_l$ and colors shown in microbubbles may also be affected by the radius $R$ and deflection $\Delta$ of the shell. To investigate such effects, we calculate the spectra and provide the simulated colors for microbubbles with the same shell thickness ($d = 900$ nm) but different deflections and radii. **Figure 3**a illustrates the calculated spectra of precursor-microbubbles with a radius of 30 µm and different deflections ($\Delta$ = 800, 700, and 600 nm). When the deflection $\Delta$ decreases from 800 to 600 nm, the top shell thickness also changes by 200 nm. However, since the change of lateral edge thickness is less than 10 nm, the spectral shift is less than 20 nm, resulting in little color change. In Figure 3b, the results are plotted for precursor-microbubbles with the same deflection ($\Delta$ = 800 nm) and different radii ($R$ = 26, 30, and 34 µm). No obvious spectral shift was observed with the increasing radius. These calculations indicate that the influence of deflection $\Delta$ and radius $R$ on the color of microbubbles is much smaller than that of shell thickness $d$. However, the increase of deflection can effectively improve the relative intensity of the emitted light from the microbubbles, agreeing well with the results shown in Figure 2e.

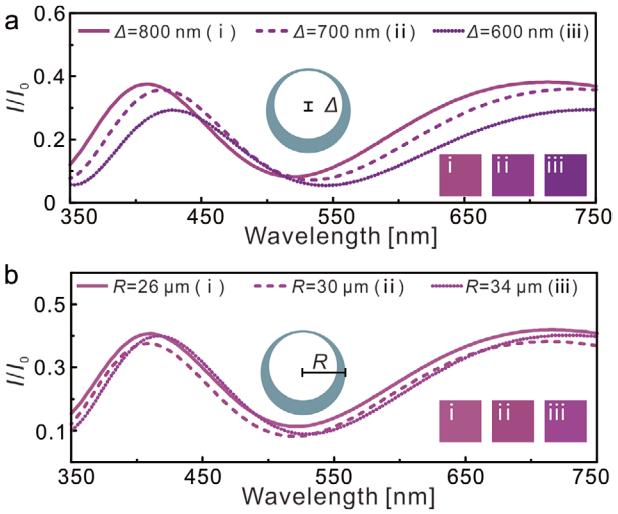


**Figure 3.** Calculated spectra of precursor-microbubbles with different a) deflections $\Delta$ and b) radii $R$, and in all conditions, average shell thickness is fixed at 900 nm. In (a), the radius is set at 30 µm and the deflection equals 800 nm in (b). The insets show the diagram of precursor-microbubbles and color lumps converted from the corresponding spectra.

### 2.4. Experimental Validation of the Theoretical Model

Experimentally, the shell of the precursor-microbubble (i.e., oil phase) may dissolve in the surrounding PVA aqueous solution. In order to keep the mass of the shell constant, the as-prepared precursor-microbubbles were transferred to oil-phase-saturated PVA solution for following characterizations. The evolution process of precursor-bubbles in the oil-phase-saturated

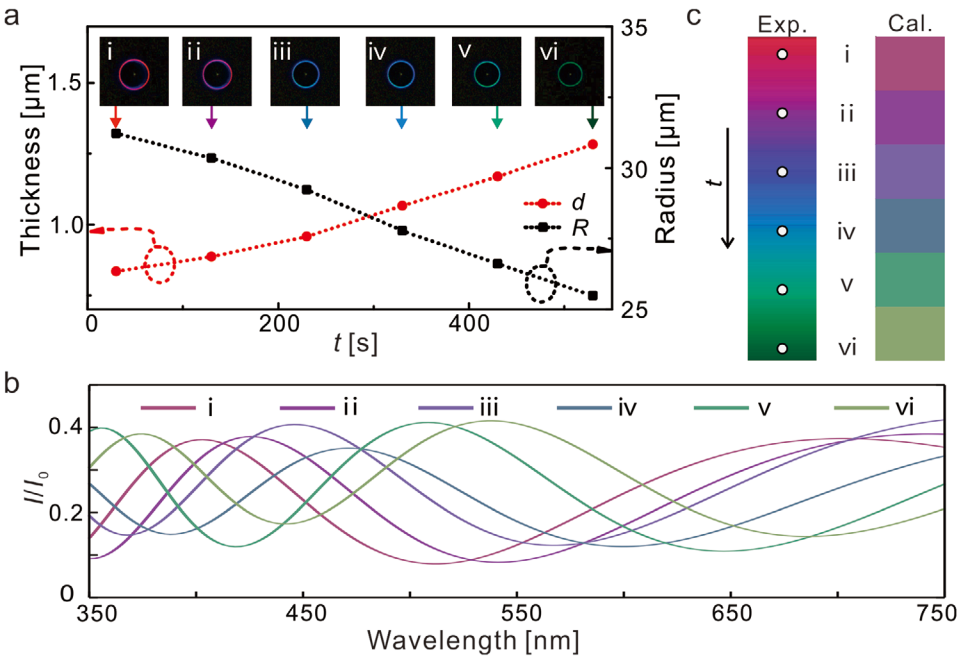


**Figure 4.** a) Radius and shell thickness variations of a single precursor-microbubble as a function of time *t*. Insets show the images of aimed bubble when *t* equals 30, 130, 230, 330, 430, and 530 s (spots i–vi). b) Calculated spectra corresponding to time spots (i)–(vi) in (a). c) Color variation comparison between experimental and calculated results. The experimental color bar consists of averaged RGB values from video frames and the six-color lumps at right were colors transformed from the calculated results based on experimental radii and thicknesses.

aqueous solution was recorded experimentally under the optical microscope for verification of the proposed model. The radius of the microbubble can be retrieved at different times by analyzing the recorded video frames ($t$ = 30, 130, 230, 330, 430, and 530 s), as shown in **Figure 4**a. It is found that precursor-microbubbles with liquid oil shells tend to gradually shrink due to inner gas dissolution. Due to their larger surface to volume ratios ($\propto 1/R$), smaller microbubbles dissolve more rapidly than bigger ones. After the gas was fully dissolved, the microbubble became an oil drop with radius $r$, so that the shell thickness $d$ of the microbubble can be calculated by equation $d = R - \sqrt[3]{R^3 - r^3}$, where the mass of the shell is considered to be constant. Assuming the remaining thickness at the bubble top as 100 nm, the deflection $\Delta$ can also be determined. Based on the geometrical data, the spectra of microbubbles can be calculated (Figure 4b) and the corresponding color lumps can then be converted (Figure 4c). Experimentally, by calculating the average RGB value for the pixels of the colorful pattern, the corresponding color bar is also obtained (see Figure 4c). It can be seen that the shell thickness of microbubbles increases with time, resulting in a significant red shift in the spectra of microbubbles. A good match between the experimental results and the calculated results has been reached, verifying the theoretical model's validity.

### 2.5. Thickness Estimation Using Developed Model

We apply the model for thickness estimation of precursor-microbubbles in an aqueous solution in light of the coloration's dependency on the shell thickness. Here, the generated precursor-microbubbles were placed in an oil-phase-unsaturated PVA aqueous solution. Thus, besides gas expelling, the slow dissolution of hydrogel precursor into the water should also lead to decrease of the shell mass and corresponding thickness. Color variation of a single precursor-microbubble along time, in this case, is shown in **Figure 5**a and Figure S7, Supporting Information. The different color-variation rates between the centered microbubble and the surrounding gathered microbubbles further prove that the color variation of the microbubbles is related to the chemical environment and the corresponding thickness evolution. With the thinning thickness, the hue of

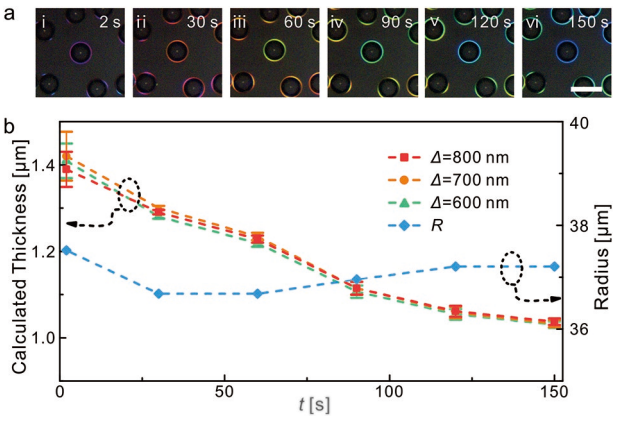


**Figure 5.** Assessment of the time-dependent thickness of a precursor-microbubble. a) Optical images of a precursor-microbubble with corresponding time spots labeled. The scale bar is 50 μm. b) Evolution of calculated thickness and experimental radius of the microbubble as a function of time.

the appearing color changed accordingly, indicating a blue shift of the corresponding spectrum. Microscope observation of the radius of the single microbubble is recorded in Figure 5b and the radius fluctuates slightly instead of showing a monotonous tendency of decreasing. We then calculated the thickness of the bubble, with three deflection values, that is, $\Delta = 600$, 700, and 800 nm, assumed. For easy thickness determination, six sets of averaged RGB values of the single bubble were extracted and converted to Hue, Saturation, Value (HSV) values. Meanwhile, the calculated spectra with three deflection values were converted to hue values. By comparing experimental and calculated hue values, we can estimate the precursor-microbubble shell thickness, and the results are shown in Figure 5b. One can see that the degree of deflection only slightly affects the estimated thickness.

## 3. Conclusion

Using glass-capillary microfluidic techniques, we fabricated precursor-microbubbles and their cured ones and structural coloration was observed. It is proved that the buoyancy-induced deflections in the microbubble shells make it possible for propagating light to experience TIR within the shell, thus enabling the formation of retro-reflected patterns under a microscope. We tried to verify the coloration mechanism by comparing the experimental color variation with the calculated results from a geometrical optical model. As a good match has been reached, the analytic model is capable of calculating the shell thickness of microbubbles and their precursors, providing a convenient method for shell thickness evaluation in a complex liquid environment. Thus, this work is meaningful for understanding the fabrication and evolution of microbubbles produced by microfluidic chips. With the guidance from such a theoretical approach, functional materials can be introduced in intentionally designed microstructure to achieve sophisticated coloration. This might have great potential in the fields of sensing, displays, and anti-counterfeiting.

## 4. Experimental Section

*Materials*: The materials include PVA (molecular weight = 13 000 – 23 000, 88% hydrolyzed, Sigma-Aldrich), MAAn (Aladdin), ethylene glycol dimethacrylate (EGDMA, Aladdin) and 2-hydroxy-2 methyl propiophenone (Darocure 1173, Aladdin), nitrogen ($N_2$). MAAn, EGDMA, and Darocure 1173 were mixed at a weight ratio of 70:20:10 and the oil mixture was then degassed with nitrogen for 15 min to remove the remaining oxygen. To prepare oil-saturated PVA aqueous solution, excess oil mixture was added to the aqueous solution. Surrounding temperature was raised to 60 °C and kept for 1 h. Then the solution was placed for 1 h to cool down and the supernatant was taken for use.

*Preparations of Precursor-Microbubbles*: To fabricate a glass capillary microfluidic chip, the glass capillaries (outer diameter = 0.96 mm, Genel Inc., Shanghai) were cleaned in acetone, ethanol, and deionized water successively with ultrasonic treatment, and then dried in $N_2$. The orifices of two cylindrical glass capillaries were tapered to around 8 and 150 µm respectively, then they were coaxially aligned inside a square capillary (inner dimension = 1.0 mm). The distance between the two orifices was about 150 µm. While operation, PVA aqueous solution (4 wt%) and MAAn mixture were delivered as continuous phase and dispersed phase respectively. The flow rates of both phases were controlled by syringe pumps (Harvard apparatus). $N_2$ was introduced first through a reducing valve, then a pressure regulator (ControlAir Inc.) to the chip as the inner phase. Polythene tube (inner diameter = 0.86 mm) was connected to the chip outlet for bubble collection, the tailing end of which was fixed to avoid pressure variation at the chip junction. The whole process was monitored using an inverted microscope (Eclipse, Nikon). The as-prepared precursor-bubbles were then transferred to oil-phase-saturated PVA solution to avoid dissolution of the shell in surrounding medium.

*Preparations of Cured Microbubbles*: The produced microbubbles were collected in a dish containing oil-phase-saturated PVA solution. After a piece of cover glass was placed on top of the surface, which obviated bubble ruptures and made it possible for bubble curing, microbubbles were exposed to UV light (365 nm, 10 W, Zhongshan Zigu Lighting Appliance Factory, China) for 3 min.

*Refractive Index Measurement*: The refractive indexes of the oil mixture and PVA aqueous solution were measured via abbe refractometer (2WAJ, Shanghai Liguang Precision Instrument Co.) at ambient temperature.

*Characterization*: The samples were observed under an optical microscope (BX51, Olympus) at reflection mode, equipped with a halogen lamp and a charged couple device (CCD) camera. Determination of radii of microbubbles was done by measuring the area that bubbles covered in software ImageJ. Morphologies of cured bubbles and fractured ones were characterized by SEM (Phenom Prox). For SEM characterization, the sample was washed with deionized water and ethanol for several times to remove excess PVA, and then got dried.

*Color Variation Recording*: To figure out the color variation pattern of microbubble, videos of microbubbles under microscope were recorded via microscope (BX51). The recorded video was then exported to TIFF images by using Adobe Premiere Pro CC 2018. Matlab scripts were defined to extract required pixels from the aimed microbubble and average RGB values of the pixels in each exported frame. Each pixel in the figure equaled to a $4 \times 1$ matrix including RGB values and transparency. Only if the maximum of RGB values were above the pre-set threshold would the corresponding pixel be extracted for calculation.

## Supporting Information

Supporting Information is available from the Wiley Online Library or from the author.

## Acknowledgements

This work was supported by the Natural Science Foundation of China (Nos. 51961145108, 61975035, and 51850410502), National Key Research and Development Program of China (2018YFA0306201), and the Science and Technology Commission of Shanghai Municipality (Nos. 19XD1400600, 20501130700, and 19JC1415500).

## Conflict of Interest

The authors declare no conflict of interest.

## Data Availability Statement

The data that support the findings of this study are available from the corresponding author upon reasonable request.

## Keywords

internal reflection, microbubbles, structural colors, thickness evaluation, thin film interference

Received: February 5, 2021
Revised: April 2, 2021
Published online:

[1] S. Kinoshita, S. Yoshioka, J. Miyazaki, *Rep. Prog. Phys.* **2008**, *71*, 076401.
[2] M. Sumetsky, Y. Dulashko, R. S. Windeler, *Opt. Lett.* **2010**, *35*, 898.
[3] M. Sumetsky, Y. Dulashko, R. S. Windeler, *Opt. Lett.* **2010**, *35*, 1866.
[4] T. Tang, X. Wu, L. Liu, L. Xu, *Appl. Opt.* **2016**, *55*, 395.
[5] H. Lin, S. Fraser, M. H. Hong, M. Chhowalla, D. Li, B. H. Jia, *Adv. Photonics* **2020**, *2*, 055001.
[6] L. Lin, X. Peng, Z. Mao, W. Li, M. N. Yogeesh, B. B. Rajeeva, E. P. Perillo, A. K. Dunn, D. Akinwande, Y. Zheng, *Nano Lett.* **2016**, *16*, 701.
[7] J. G. Ortega-Mendoza, J. A. Sarabia-Alonso, P. Zaca-Morán, A. Padilla-Vivanco, C. Toxqui-Quitl, I. Rivas-Cambero, J. Ramirez-Ramirez, S. A. Torres-Hurtado, R. Ramos-García, *Opt. Express* **2018**, *26*, 6653.
[8] N. Vogel, S. Utech, G. T. England, T. Shirman, K. R. Phillips, N. Koay, I. B. Burgess, M. Kolle, D. A. Weitz, J. Aizenberg, *Proc. Natl. Acad. Sci. USA* **2015**, *112*, 10845.
[9] M. Xiao, Z. Y. Hu, Z. Wang, Y. W. Li, A. D. Tormo, N. L. Thomas, B. X. Wang, N. C. Gianneschi, M. D. Shawkey, A. Dhinojwala, *Sci. Adv.* **2017**, *3*, e1701151.
[10] Y. Geng, J.-H. Jang, K.-G. Noh, J. Noh, J. P. F. Lagerwall, S.-Y. Park, *Adv. Opt. Mater.* **2018**, *6*, 1700923.
[11] Y. W. Shan, L. Q. You, H. K. Bisoyi, Y. J. Yang, Y. H. Ge, K. J. Che, S. S. Li, L. J. Chen, Q. Li, *Adv. Opt. Mater.* **2020**, *8*, 2000692.
[12] A. E. Goodling, S. Nagelberg, B. Kaehr, C. H. Meredith, S. I. Cheon, A. P. Saunders, M. Kolle, L. D. Zarzar, *Nature* **2019**, *566*, 523.
[13] K. Ferrara, R. Pollard, M. Borden, *Annu. Rev. Biomed. Eng.* **2007**, *9*, 415.
[14] S. Hernot, A. L. Klibanov, *Adv. Drug Delivery Rev.* **2008**, *60*, 1153.
[15] A. L. Klibanov, *Bioconjugate Chem.* **2005**, *16*, 9.
[16] F. Yang, H. Cui, Y. Liu, L. Yang, Y. Li, P. Chen, N. Gu, *Phys. Procedia* **2015**, *70*, 1074.
[17] T. Brugarolas, F. Tu, D. Lee, *Soft Matter* **2013**, *9*, 9046.
[18] S. J. Yeo, M. J. Oh, H. M. Jun, M. Lee, J. G. Bae, Y. Kim, K. J. Park, S. Lee, D. Lee, B. M. Weon, W. B. Lee, S. J. Kwon, P. J. Yoo, *Adv. Mater.* **2018**, *30*, 1802997.
[19] C. Cohen, B. Darbois Texier, E. Reyssat, J. H. Snoeijer, D. Quere, C. Clanet, *Proc. Natl. Acad. Sci. USA* **2017**, *114*, 2515.
[20] G. Debrégeas, P. G. de Gennes, F. Brochard-Wyart, *Science* **1998**, *279*, 1704.
[21] G. Y. Gor, A. E. Kuchma, *J. Chem. Phys.* **2009**, *131*, 034507.
[22] G. M. Hansen, *Appl. Opt.* **1985**, *24*, 3214.
[23] A. T. Oratis, J. W. M. Bush, H. A. Stone, J. C. Bird, *Science* **2020**, *369*, 685.
[24] B. Mandracchia, Z. Wang, V. Ferraro, M. M. Villone, E. Di Maio, P. L. Maffettone, P. Ferraro, *Light: Sci. Appl.* **2019**, *8*, 20.
[25] Y. D. Afanasyev, G. T. Andrews, C. G. Deacon, *Am. J. Phys.* **2011**, *79*, 1079.
[26] A. Utada, E. Lorenceau, D. R. Link, P. D. Kaplan, H. A. Stone, D. A. Weitz, *Science* **2005**, *308*, 537.
[27] J. K. Nunes, S. S. H. Tsai, J. Wan, H. A. Stone, *J. Phys. D: Appl. Phys.* **2013**, *46*, 114002.
[28] P. B. Duncan, D. Needham, *Langmuir* **2004**, *20*, 2567.
[29] T. Brugarolas, B. J. Park, M. H. Lee, D. Lee, *Adv. Funct. Mater.* **2011**, *21*, 3924.
[30] P. D. Howell, *J. Eng. Math.* **1999**, *35*, 251.
[31] P. J. Shopov, P. D. Minev, I. B. Bazhlekov, Z. D. Zapryanov, *J. Fluid Mech.* **1990**, *219*, 241.
[32] M. H. Lee, V. Prasad, D. Lee, *Langmuir* **2010**, *26*, 2227.
[33] N. M. Aybers, *Heat Mass Transfer* **1974**, *7*, 173.
[34] B. A. Puthenveettil, A. Saha, S. Krishnan, E. J. Hopfinger, *Phys. Fluids* **2018**, *30*, 112105.
[35] S. S. Datta, S. H. Kim, J. Paulose, A. Abbaspourrad, D. R. Nelson, D. A. Weitz, *Phys. Rev. Lett.* **2012**, *109*, 134302.
[36] M. Born, E. Wolf, E. Hecht, *Phys. Today* **2000**, *53*, 77.
[37] M. Ohmi, M. Haruna, *Opt. Rev.* **2003**, *10*, 478.